A simple finite element model to study the effect of plasma plume expansion on the nanosecond pulsed laser ablation of aluminum

Yeqing Wang[1] · David W. Hahn[2,3]

Abstract

In this paper, a simple model was proposed using finite element analysis (FEA) with a commercial FEA software ABAQUS to simulate the two-dimensional (2-D) laser heat transfer in an aluminum material. Without relying on the conventional hydrodynamic model, the proposed model not only predicts the evolutions of the temperature field and ablation profiles in the target material, but also provides an estimation on the evolutions of electron density, plasma temperature, and plasma absorption coefficient. The assumptions used in the model include the local thermal equilibrium and additional assumptions regarding the average plasma temperature and vapor density. The assumptions allowed the laser heat transfer equation to be solved together with the Saha–Eggert equation and conservation equations of matter and charge. When compared to the existing hydrodynamic models, the proposed model solves a less number of nonlinear equations and hence is computationally more efficient. The proposed FE model was employed to study the plasma-shielding effect on PLA produced by a 193 nm Excimer laser and a 266 nm Nd:YAG laser. The predictions of ablation depths, electron density, and plasma temperature agree well with the experimental data. Moreover, effects of the laser intensity and the average plasma temperature on the efficiency of the plasma shielding during PLA were also investigated and discussed in this study.

1 Introduction

Technologies based on pulsed laser ablation (PLA) have grown rapidly over the past few decades as evidenced by its increasing applications in advanced machining [1], nano-material manufacturing [2, 3], material surface processing [4, 5], thin-film deposition [6], medical surgery [7], and chemical analysis [8]. The significant advancement of these technologies is a result of the numerous research efforts that have been continuously devoted to understanding the fundamental laser ablation mechanisms. When a high-intensity laser beam is directed onto a surface of a material, the surface of the material absorbs energy from the laser beam causing a rapid temperature rise of the surface. With the increasing temperature, material quickly melts and leaves

the surface due to different ablation mechanisms, such as evaporation and material phase explosion [9–13]. When the laser intensity exceeds the optical breakdown threshold of the material, a plasma plume is formed above the material surface owing to the ionization of the material [8, 14]. The formation and expansion of the plasma plume result in an attenuation of the actual laser energy that delivers to the material surface as the incident laser beam transmits through the plasma plume. Such a phenomenon is known as the plasma-shielding effect. Meanwhile, the evaporation of mass from the material surface produces a shockwave, which also influences the overall ablation process [15]. Therefore, laser ablation is a complex problem that involves laser–material interaction, laser–plasma interaction, plasma–material interaction, as well as shock wave–material interaction. Despite continuous research efforts, the fundamental laser ablation mechanisms are still widely unexplored [16]. This paper, in particular, focuses on the plasma-shielding effect during the PLA process.

Research efforts related to the plasma-shielding effect of PLA based on experimental measurements have greatly expanded the understanding of the laser ablation mechanisms due to the development of novel experimental techniques, such as the time-resolved shadowgraphy [11, 17,

✉ Yeqing Wang
  yw253@msstate.edu

1 Aerospace Engineering Department, Mississippi State University, Mississippi State, MS 39762, USA

2 Mechanical and Aerospace Engineering Department, University of Florida, Gainesville, FL 32611, USA

3 Present Address: Aerospace and Mechanical Engineering Department, University of Arizona, Tucson, AZ 85721, USA

18] and spectrally integrated time-resolved imaging [13, 19, 20]. Using these techniques, temporal evolutions of the mass removal, plasma plume formation, and shock wave propagation were successfully captured with images taken at nanosecond scales. Furthermore, time-resolved pump-probe experimental techniques have been developed to measure the absorption characteristics of the plasma shielding during the laser ablation through a direct comparison between the incident and transmitted laser intensities [21]. Advanced spectroscopic experimental methods [18, 22, 23] have also be adopted to estimate the evolutions of the electron density, temperature, pressure, and length of the plasma. These experimental investigations have provided direct evidences for the plasma formation and evolution, and hence, expanded our knowledge on the laser ablation mechanisms [18]. Meanwhile, they have also provided a considerable number of experimental data for model validations.

Mathematical models of PLA have been developed generally based on two approaches. The first approach is to consider the laser source as a volumetric heat flux and solve the heat transfer equation in the target material [24–28]. Using this approach, the evolution of the temperature field can be predicted and the material removal due to evaporation and material phase explosion can be estimated. The second approach is to couple the breakdown plasma model and the laser heat transfer model together through solving the hydrodynamic equations for the plasma domain and the heat transfer equation for the material domain, where the hydrodynamic equations have to be supplemented by additional equations of state [29–35]. Using this approach, not only the evolution of the target to evaporated material, but also the evolution of the target to ionized material (i.e., the plasma plume), as well as the plasma pressure can be predicted at a given laser intensity. When compared to the first approach, the second approach focuses more on the predictions of the laser-induced plasma, and requires to solve a number of nonlinear equations which poses significant challenges on the numerical implementation. A common feature of the early laser heat transfer models used in both approaches is that the shape change of the target material due to the progressive material removal was not solved as part of the solution, but only the temperature was solved. The amount of melted or vaporized material was estimated by checking the evolution of the predicted temperature field. However, in the actual PLA process, as the material progressively leaves the surface of the material, the remaining surface (i.e., the crater hole) is directly exposed to the laser beam, and hence, the laser heat flux loading condition needs to be updated simultaneously with the progressive material removal. To account for that a finite element (FE) model of PLA considering the material moving front was proposed in authors' early work [27], which allows to solve the shape change, and hence, the ablation profile of an aluminum target simultaneously with

the temperature field. Another common feature of the laser heat transfer models based on the first approach is that they consider the plasma-shielding effect by changing the laser intensity using a semi-empirical equation [9, 25, 26, 36, 37]. Parameters in such a semi-empirical equation are often difficult to obtain (discussed in detail in Sect. 2.1). Moreover, these models are unable to calculate the evolutions of the plasma temperature and electron density. To overcome these limitations, an improved FE model is proposed in this paper enabling our FEA model of PLA [27] with the capability of estimating the plasma temperature and electron density together with the temperature and ablation in the target materials. The model solves the laser heat transfer equation together with the Saha–Eggert equation, conservation equations of matter, and charge under appropriate assumptions. When compared to the hydrodynamic model (i.e., the aforementioned second approach), our FE model solves a less number of nonlinear equations and provides an acceptable estimation on the plasma temperature and electron density, and thus, is computationally more efficient and shows some advantages for rapid engineering applications. The proposed model was employed to study the plasma-shielding effect on the nanosecond PLA with aluminum targets. Results include the comparison of ablation depths predicted with and without considering the plasma-shielding effect and the PLA experimental test data, transmission ratios of the laser energy at different plasma temperatures and different laser intensities, and the evolutions of electron density and absorption coefficients.

The remainder of this paper is organized as follows: Sect. 2 provides the mathematical equations for the laser heat transfer models, a review of traditional modeling methods to study the plasma-shielding effect of PLA, and the equations used in the proposed FE model. Section 3 introduces the numerical implementation of the proposed FE model using ABAQUS with multiple user subroutines. Section 4 provides our simulation results, comparisons of predictions with experimental data, and discussions. Finally, Sect. 5 contains some conclusion remarks.

2 Modeling equations

2.1 Laser heat transfer equations

The equation for modeling heat conduction in the target material due to PLA used in many prevalent thermal models [9, 24, 25, 27, 31, 32, 36–38] is written as

$$\rho C_{\mathrm{p}}\left(\frac{\partial T}{\partial t} - \dot{s}\frac{\partial T}{\partial z}\right) - \nabla \cdot (k\nabla T) = (1 - R)\alpha I(t)\exp\left(-\alpha z'\right),$$

(1)

where ρ, C_{p}, and k are density, specific heat, and thermal conductivity of the target material, respectively. Note that these material parameters are all temperature-dependent. t and T denote time and temperature, respectively. $\dot{s}$ is the surface recession rate. z is the coordinate normal to the recession surface. On the right-hand side, R and α are the reflectivity and absorption coefficient of the target surface, both temperature-dependent. z' denotes the vertical distance from any points within the target material to the surface, i.e., $z' = z - \Delta z(t)$, where $\Delta z(t)$ is the ablation depth (see Fig. 1). $I(t)$ denotes the laser intensity reaching the target surface, and can be expressed using

$$I(t) = I_0(t) \exp\left[-\tau(t)\right], \tag{2}$$

where $I_0(t)$ is the incident laser heat flux and $\tau(t)$ denotes the optical thickness. The exponential term denotes the attenuation of the laser intensity when it transmits through the laser-induced plasma. The different models of the optical thickness are discussed in detail in Sect. 2.2.

In Eq. (1), the ablation rate $\dot{s}$ under low laser irradiance conditions when material is removed primarily by evaporation can be modeled using the Hertz–Knudsen equation:

$$\dot{s} = \frac{\beta}{\rho}\sqrt{\frac{m}{2\pi k_{\mathrm{B}}T_{\mathrm{s}}}}p_{\mathrm{vap}}, \qquad T_{\mathrm{s}} \leq 0.8T_{\mathrm{c}}, \tag{3}$$

where β is the vaporization coefficient, ρ is the local density at the target surface, m is the atomic mass of the target material in kg, k_{B} is the Boltzmann constant, T_{s} is the temperature at the target surface, and p_{vap} denotes the vapor pressure which can be calculated by integrating the Clausius–Clapeyron equation:

$$p_{\mathrm{vap}} = P_{\mathrm{b}} \exp\left[\frac{mL_{\mathrm{v}}}{k_{\mathrm{B}}}\left(\frac{1}{T_{\mathrm{b}}} - \frac{1}{T_{\mathrm{s}}}\right)\right], \tag{4}$$

where P_{b} and T_{b} are the boiling temperature and the boiling pressure, respectively, and L_{v} is the latent heat of vaporization in J/kg.

Under high laser irradiance conditions, when the resulting surface temperature exceeds $0.75 \sim 0.9 \cdot T_{\mathrm{c}}$ (T_{c} being the critical temperature of the material) [39], it is believed that the homogenous bubble nucleation starts to take place in the molten pool and the liquid experiences large density fluctuations [4, 10, 12, 39–42]. When the bubbles reach a critical radius R_{c}, they start to grow spontaneously and burst, leading to liquid droplets and vapor and hence a rapid increase of ablation rate. Such a phenomena is known as material phase explosion. The ablation rate $\dot{s}$ when phase explosion occurs can be approximated using

$$\dot{s} = \frac{\beta}{\rho}\sqrt{\frac{m}{2\pi k_B T_s}}p_{vap} + I_n\chi(t)\frac{4\pi}{3}R_c^3\rho_v, \qquad T_s > 0.8T_c, \tag{5}$$

where the first and second terms on the right side of the equation denote the contributions of material evaporation and phase explosion, respectively. I_{n} is the rate of homogenous nucleation, $\chi(t)$ is the thickness of the superheated layer (i.e., the material, where the temperature is above $0.75 \sim 0.9 \cdot T_{\mathrm{c}}$). R_{c} is the critical radius of vapor bubbles and ρ_{v} is the density of the superheated liquid or vapor. It should be mentioned that, in this study, we focused on the fundamental case with low laser energy for which the ablation rate was modeled using Eqs. (3) and (4). In other words, the ablation rate in Eq. (5) for high laser energy condition was not used. Future study will be carried out to investigate the effect of plume expansion under high laser energy conditions.

The initial and boundary conditions of the current laser heat transfer model are the same as those described in our early work [27, 43] and hence are omitted here.

2.2 Equations for modeling the plasma-shielding effect

The plasma plume formed above the target surface (see Fig. 1) absorbs part of the laser energy when the laser beam propagates through the plasma before it actually delivers to the target surface. The attenuation of the laser energy results in less efficient target heating and ablation, which is known as the plasma-shielding effect.

2.2.1 Review of equations for the plasma-shielding effect in current laser ablation thermal models

Currently, a number of laser ablation models have been reported that can account for the plasma-shielding effect [9, 25, 26, 28, 36, 37]. For models that mostly focus on the temperature and heat conduction in the target material, the plasma-shielding effect is considered in the formulation
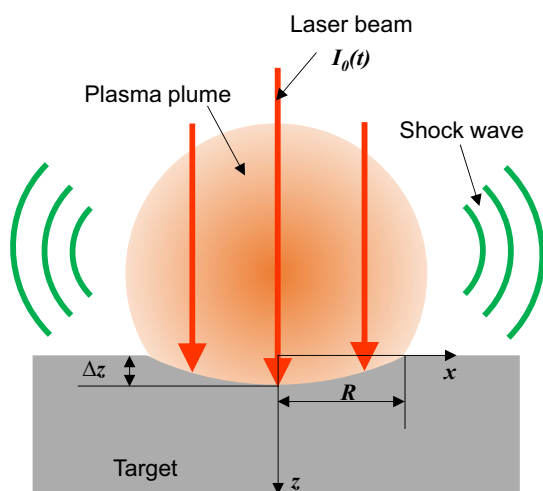

Fig. 1 Illustration of laser interaction with a solid target material, where $I_0(t)$ denotes the incident laser heat flux

by substituting the transmitted laser intensity (Eq. (2)) into the heat transfer governing equation (Eq. (1)). The optical thickness $\tau(t)$ in Eq. (2) used in many of the current models adopts the expression first proposed by Bulgakov and Bulgakova [36], written as

$$\tau(t) = a\Delta z(t) + bE_a(t), \qquad (6)$$

where a and b are time-independent coefficients, units in m^{-1} and $m^2\,J^{-1}$, respectively, $\Delta z(t)$ is the ablation depth, and $E_a(t)$ is the absorbed energy by plasma in $J\,m^{-2}$. Such an equation is derived by assuming that the absorption is proportional to the particle density and the irradiation spot is much larger than the size of the vaporized cloud. It is also limited to the case of moderate absorption [9, 36, 37]. The coefficients a and b are derived from equations:

$$a = \frac{\rho f(T_v)}{m}, \quad b = (\gamma - 1)\frac{\partial f}{\partial T}\bigg|_{T_v} k_B^{-1}, \qquad (7)$$

where T_v is the vaporization temperature and assumed to be a constant, $f(T_v)$ is the rising function of temperature (specific to each kind of particle), and γ is the effective adiabatic exponent. Although equations for coefficients a and b are provided, the explicit form of the rising function $f(T_v)$ is often not available. Therefore, using Eq. (6) to directly obtain coefficients a and b is challenging. Bulgakov and Bulgakova [36] recommended to select coefficients a and b by fitting the predicted vaporized mass ($M = \rho S\Delta Z$, where S is the vaporized area and ΔZ is the total vaporized mass per pulse) using the experimental data. This is a trial-and-error calibration procedure, which means that users need to pick different guesses of coefficients a and b for calculations until they find a set that can best ensure the agreement between the calculation and the experimental data. It is also recommended to determine coefficient a first using a low laser intensity when the absorbed energy is small and the second term in Eq. (6) can be ignored. When a is known, the coefficient b can then be found by ensuring the agreement between the calculation and the experimental data at higher laser intensity conditions. In other words, to determine coefficients a and b, sufficient experimental data need to be provided from low laser intensity to high laser intensity conditions.

In addition to coefficients a and b, the absorbed energy E_a in Eq. (6) also needs to be determined. Unlike coefficients a and b which are constant parameters, the absorbed energy E_a is time-dependent and thus needs to be determined at

each time increment, although Eq. (6) has been adopted in many current laser ablation models [25, 26, 28]. However, to author's knowledge, the exact functions (values or curves) for E_a used in those models have barely been reported. To determine E_a, it is recommended also to use the trial-and-error procedure [36]. Moreover, the choice of E_a needs not only to ensure the agreement between the calculation and the experimental data of vaporized mass, but also satisfy the self-consistent equation:

$$E_a(t) = \int_0^t I_0(t')\left[1 - \exp\left(-\tau(t')\right)\right]dt'. \qquad (8)$$

Despite significant simplifications, the trial-and-error procedure used for determining the parameters in Eq. (6) can be quite time consuming. Furthermore, these models only focus on the effect of plasma shielding on the temperature and ablation response of the target material, the evolutions of the plasma temperature, and electron density cannot be predicted.

2.2.2 Review of equations for the plasma-shielding effect in current hydrodynamic laser ablation plume expansion models

Another prevalent type of laser ablation models focuses on the expansion of the plasma plume by solving the Euler equations of hydrodynamics (i.e., the conservation equations of mass, momentum, and energy) and the ideal gas law. These models predict the density, pressure, velocity, internal energy, and temperature of the vapor at each spatial point of the plume [29, 31, 32, 34, 35]. Some of these models also account for the formation of a plasma of the evaporated material by coupling the hydrodynamic equations with the Saha–Eggert equation, internal energy equation, and the equations of the conservation of matter and charge [31, 32]. They are valid under the assumption of local thermal equilibrium (LTE), which means that thermal equilibrium is established between electrons, neutrals, and ions, and temperatures of all particles are the same in a sufficiently small region of the plume. The coupling of the additional equations of state allow the hydrodynamic model to calculate the plasma temperature, number densities of electrons, neutral, and multiply charged ions. Using these parameters, the laser energy absorbed by the plasma due to the inverse Bremsstrahlung (IB) effect when the laser travels through the plasma can be characterized using the absorption coefficient, expressed as

$$\alpha_{IB,e-n} = \left[1 - \exp\left(-\frac{hc}{\lambda k_B T}\right)\right]Qn_e n_0,$$

$$\alpha_{IB,e-i} = \left[1 - \exp\left(-\frac{hc}{\lambda k_B T}\right)\right]\frac{4e^6\lambda^3 n_e}{3hc^4 m_e}\left(\frac{2\pi}{3m_e k_B T}\right)^{1/2}(Z_1^2 n_{i1} + Z_2^2 n_{i2}),$$

$$(9)$$

where $\alpha_{IB,e-n}$ and $\alpha_{IB,e-i}$ denote the absorption coefficients due to electron–neutral IB and electron–ion IB effect, respectively. h is the Planck constant, c is the speed of light, λ is the laser wavelength, Q is the cross section for photon absorption by an electron, during a collision with neutrals, $Q = 10^{-36}$ cm^5, T is the plasma temperature, e is the elementary charge, m_e is the electron mass, and n_e, n_0, n_{i1}, and n_{i2} denote the number densities of electron, neutral, singly charged ion, and doubly charged ion, respectively. Z_1 and Z_2 are the charge number, $Z_1 = 1$, and $Z_2 = 2$. Cautious need to be taken when using Eq. (9), and all parameters need to use the CGS unit system. The resulting unit of $\alpha_{IB,e-n}$ and $\alpha_{IB,e-i}$ is cm^{-1}.

Some of the hydrodynamic models are also coupled with the heat conduction in the target material [29, 31, 32]. Rather than making assumptions of averaged surface temperature, these models solve the heat conduction equation first and then use the obtained material surface temperature as a boundary condition in the hydrodynamic model to predict the density, velocity, pressure, and temperature of the plasma plume. At the same time, the formation of the plume absorbs part of the energy from laser beam and leads to a reduction of the actual energy delivered to the target surface. Therefore, the absorption coefficient obtained from Eq. (9) needs to be passed back to the heat conduction Eq. (1) to account for the loss of the laser energy using

$$I(t) = I_0(t) \exp\left(-\int_0^\infty \alpha_{IB} dz\right), \tag{10}$$

where α_{IB} is the total absorption coefficient and $\alpha_{IB} = \alpha_{IB,e-n} + \alpha_{IB,e-i}$.

These models pose significant challenges on the numerical implementation which often requires to solve at least nine nonlinear equations (depending on the number of multiply charged ions) simultaneously in a coupled manner. Due to the complexity of these models, the geometry of the problem is often restricted to one dimension (1-D). Another common feature of these models is that they are often developed using custom-written codes, which make researchers difficult to reproduce and hence verify simulation results. Many papers only present the mathematical equations and simulation results without providing details on the numerical implementations. In addition, when dealing with the coupling of fluid (i.e. the hydrodynamic model) and structure (i.e., the heat conduction of target material) for laser ablation problems, the progressive material removal leads to a continuous geometry change for both the fluid and structure domains, and hence moving boundary conditions for both formulations. Accounting for moving boundary conditions in the fluid–structure-coupled model can be extremely challenging, especially for problems with two- and three-dimensional (2-D and 3-D) geometries.

Table 1 Constant parameters used in the FEA simulation

Parameter	Value	Unit
Boltzmann constant	$k_B = 1.3865 \times 10^{-16}$	erg/K
Elementary electrical charge	$e = 4.803 \times 10^{-10}$	Fr
Mass of electron	$m_e = 9.109 \times 10^{-28}$	g
Mass of Al atom	$m = 4.48 \times 10^{-23}$	g
Planck's constant	$h = 6.626 \times 10^{-27}$	erg.s
Speed of light	$c = 2.9979 \times 10^{10}$	cm/s
Laser wavelength	$\lambda = 193 \times 10^{-7}$	cm
First ionization potential of Al	$IP_1 = 5.98$	eV
Second ionization potential of Al	$IP_2 = 18.863$	eV

2.2.3 Proposed simple finite element model of PLA considering the plasma-shielding effect

As discussed above that both the thermal and the hydrodynamic models considering the plasma-shielding effect may seem quite difficult to implement. In this paper, a model using finite element analysis (FEA) with a commercial general-purpose FEA software ABAQUS is proposed. The ionization and IB absorption are considered in the model. For the nanosecond laser ablation of aluminum, the IB process is considered to be the most important mechanism of the plume absorption [9, 44, 45]. To investigate the plasma effect on the laser heat conduction, the absorption coefficient Eq. (9) is estimated following the procedures described below and then passed into the heat conduction equation by substituting Eq. (10) into Eq. (1).

Here, the plasma plume is assumed to be in local LTE and considered nonviscous and electrically neutral, containing five species (Al, Al$^+$, Al^{2+}, Al^{3+}, and e). Such an assumption has also been used in many other studies [31, 32]. Under this assumption, the ionization degree of the plasma (i.e., fractions of electrons and ions) can be approximated using the Saha–Eggert equation [32, 33]:

$$\frac{x_e x_{i1}}{x_0} = \frac{1}{n_{vap}} \left(\frac{2\pi m_e k_B T}{h^2}\right)^{3/2} \exp\left(-\frac{IP_1}{k_B T}\right), \tag{11}$$

$$\frac{x_e x_{i2}}{x_{i1}} = \frac{1}{n_{vap}} \left(\frac{2\pi m_e k_B T}{h^2}\right)^{3/2} \exp\left(-\frac{IP_2}{k_B T}\right), \tag{12}$$

where n_{vap} denotes the total vapor number density, and $n_{vap} = \rho_{vap}/m$ with ρ_{vap} being the vapor density and m being the atomic mass. x_e, x_0, x_{i1}, and x_{i2} denote the fractions of number densities of electron, neutral, singly charged ion, and doubly charged ion, respectively, and $x_i = n_i/n_{vap}$, for

$i = $ e, 0, i1, and i2. IP_1 and IP_2 are the first and second ionization potentials of the target material (see Table 1).

To calculate the four unknowns x_e, x_0, x_{i1}, and x_{i2}, two additional equations, the conservation equations of matter and charge, need to be provided:

$$x_0 + x_{i1} + x_{i2} = 1, \tag{13}$$

$$x_{i1} + 2x_{i2} = x_e. \tag{14}$$

The number densities of the particles n_e, n_0, n_{i1}, and n_{i2} can be obtained by solving the nonlinear equation set (11)–(14) providing the plasma temperature T and the density of the vapor ρ_{vap} at all points within the plasma. To get an accurate prediction of the temperature and the vapor density at the local equilibrium, an energy balance needs to be applied, either locally or globally on the plasma plume. In other words, both the energy balance in the plasma domain and the energy balance in the solid domain (i.e., the heat transfer) need to be solved at the same time. Unfortunately, ABAQUS does not allow such two energy balance equations to be solved simultaneously. To overcome this limitation, we assumed that an averaged plasma temperature T_{avg} and an averaged vapor density $\rho_{vap-avg}$ are representative of the spatially varying plasma temperature and the vapor density and can be used in the Saha–Eggert equation to obtain the averaged particle densities in the plume. The averaged plasma temperature and vapor density can be calculated directly by solving the sole energy balance in the solid domain under appropriate assumptions, and thus eliminating the need to solve the second energy balance in the plasma domain, which reduced the complexity of the problem and makes the numerical implementation possible in ABAQUS. Here, the assumption of using the averaged plasma temperature and vapor density can be justified by the experimental data reported in Ref. [23], where it was found that the electron density is spatially homogenous along the laser beam axial before 0.8 μs. In other words, the spatial distributions of the plasma temperature and vapor density have insignificant effects on the spatial distribution of the electron densities during the initial plasma expansion. Experimental tests with tomography or camera imaging have proved that the plasma temperature is hot in the center and cooler away from the center [17, 19, 20]. The temperature near the target surface is about 50% of the peak temperature in the center of the plasma, as evidenced by the experimental data and theoretical calculations [19]. Assuming that the plasma temperature near the solid surface equals the surface temperature of the target, the average plasma temperature can be estimated using $T_{avg} = 1.5T_s$. Such an assumption has been justified and the justification will be discussed in detail in Sect. 4.2. Furthermore, the average density of the vapor is estimated using $\rho_{vap-avg} = \Delta m / V_{plume}$, where Δm is the vaporized mass and V_{plume} is the volume of the plasma plume. Assuming

that the removed material is completely vaporized and the in-plane ablation profile is circular, then according to the mass conservation, the vaporized mass can be estimated by

$$\Delta m = \rho \sum \Delta z(x) \Delta x^2, \tag{15}$$

where is ρ the density of aluminum, $\Delta z(x)$ is the ablation depth (see Fig. 1), and Δx is the infinitesimal length in the in-plane direction. The volume of the plasma plume V_{plume} can be calculated by assuming the plasma to be a sphere. It has been reported that although the plasma expands, the plasma shape remains spherical from ignition up to 200 ns due to homogeneous heating of the plume by the energetic species (electrons and ions) [19]. After that, the expansion becomes anisotropic and the plasma shape becomes hemispheric [19, 23]. In this study, the pulse duration is 12 ns and the cooling step is 350 ns. We assume that the plasma shape remains spherical throughout the analysis. According to Sedov's model [46], the expansion of the plume diameter follows $D_{plume} = \delta t^{0.4}$, where δ is a coefficient that depends on the laser wavelength. Here, δ is chosen as 0.9 by curve fitting the experimental data for wavelengths of 266 nm and 193 nm [23]. Note that here, the unit of D is mm and t is μs. The volume of the plasma plume is $V_{plume} = \frac{1}{6}\pi D_{plume}^3$.

After the average plasma temperature T_{avg} and vapor density $\rho_{vap-avg}$ are obtained, they are plugged into Eqs. (11)–(14) to calculate the average particle number densities. Then, the average absorption coefficient can be obtained with Eq. (9) and used further to calculate the attenuation of the laser energy by Eq. (10).

3 Numerical Implementation

The numerical procedure for modeling the nanosecond PLA without considering the plasma-shielding effect using FEA has been introduced in authors' early work [27, 43, 47]. Such a procedure can also be extended or modified for modeling the lightning strike ablation [48–50], the charring ablation [51], and the laser additive manufacturing heat transfer [52]. The highlights of this numerical procedure are the coupling between the laser heat conduction and the progressive material removal through the development of DFLUX and UMESHMOTION subroutines, as well as the adoption of Arbitrary Lagrangian–Eulerian (ALE) algorithm. In particular, the DFLUX subroutine was developed to define the volumetric laser heat flux (i.e., the heat source term on the right-hand side of Eq. (1)) and the surface heat loss due to vaporization. The UMESHMOTION subroutine was developed to capture the shape change due to the progressive material removal after each time increment. The ALE algorithm enabled automatic re-meshing after the geometric

shape change due to the progressive material removal. The readers are referred to our previous work for detailed information regarding these subroutines.

In this study, our previous numerical procedure [27, 43] was modified to account for the plasma-shielding effect. First, the number densities of electron, neutral, and ions (n_e, n_0, n_{i1}, and n_{i2}) were solved from four nonlinear equations, i.e., Eqs. (11)–(14), and $x_i = n_i/n_{vap}$ at each time increment. To solve such a nonlinear equation system, additional utility subroutines were developed based on the open source Fortran nonlinear system of equations solver published on GitHub (URL: https://github.com/yoki/Optimization). The two most important parameters for such a nonlinear equation system, i.e., the average plasma temperature and density of the plasma plume, were first calculated in the DFLUX subroutine and then passed to these utility subroutines. The constant parameters, including electron mass, Boltzmann constant, Planck constant, atomic mass of aluminum, and the first and second ionization potential of aluminum are listed in Table 1. Second, the calculated average number densities of different particles (n_e, n_0, n_{i1}, and n_{i2}) were passed back to the DFLUX subroutine to calculate the absorption coefficient of the plasma with Eq. (9). Finally, the calculated absorption coefficient, α_{IB}, was used to obtain the actual laser intensity that reaches to the target surface with Eq. (10). Note that all the aforementioned calculations were performed at each time increment and the data transfer between different subroutines was achieved using Fortran common blocks. The average computational time is about 4–5 h on a laptop with dual core and 16 Gb RAM.

The target material used in this study is pure aluminum (Al). Such a choice is because both the pulsed laser ablation experimental data under different laser conditions (i.e., different wavelengths and irradiances) and the temperature-dependent material properties for pure aluminum are available in the literature [4, 10, 24, 29, 34, 35, 39, 53, 54], which

are essential elements for validating the proposed model. The material properties, including the thermal conductivity, specific heat, density, absorption coefficient, and reflectivity, are temperature-dependent and the same as those presented in authors' early work [27, 43]. Here, they are listed in Tables 2 and 3. It is worth mentioning that the absorption coefficient and the reflectivity of the aluminum target were calculated using the refractive index of the material based on the Drude's model [24]. The detailed calculated procedure can be found in Ref. [24]. In addition, the dimension of the target material, computational domain, mesh size, and computer configurations for the proposed 2D model were also the same as those described in authors' early work.

4 Results and discussions

The laser source used in the proposed FE model is a 193 nm Excimer laser and a 266 nm Nd:YAG laser. The corresponding durations of the laser pulses are 12 ns and 6 ns, respectively. Both laser pulses were followed by a cooling step with a duration of 350 ns in ambient. Such a duration is chosen, such that the completion of the ablation followed

Table 3 Absorption coefficients and reflectivity of aluminum under 266 nm laser [27]

Temperature (K)	Absorption coefficient (1/m)	Reflectivity (%)
300	3.83×10^8	80.00
933	3.83×10^8	77.20
2000	3.55×10^8	72.47
4000	3.01×10^8	63.61
6000	2.48×10^8	54.75
8860	3.83×10^6	42.07

Table 2 Material properties of aluminum used in the simulation

Material property		Temperature	Unit
Melting temperature	$T_m = 933$ [24]		K
Critical temperature	$T_c = 8860$ [39]		K
Critical density	$\rho_c = 300$ [39]		kg/m³
Density	$\rho = 2700$ [24]	$T \leq T_m$	kg/m³
	$\rho = \rho_c (1 + 0.75(1 - T/T_c) + 3(1 + T/T_c)^{1/3})$ [24]	$T_m < T \leq T_c$	kg/m³
Specific heat	$C_p = 0.5203\,T + 643.9$ [27]	$T \leq T_m$	J/(kg·K)
	$C_p = 1160$ [27]	$T_m < T \leq T_c$	J/(kg·K)
Thermal conductivity	Data from Ref. [35]		W/(m·K)
Boiling temperature	$T_b = 2743$ [4]		K
Boiling pressure	$P_b = 1.01 \times 10^5$ [34]		Pa
Vaporization coefficient	$\beta = 0.82$ [59]		
Latent heat of vaporization	$L_v = 10.78$ [4]		MJ/kg

by the removal of the laser pulse is ensured based on our preliminary simulation trials. The laser beam is a Gaussian beam with a spatial profile of $\dot{q} \exp\left(-7.6x^2/r^2\right)$, where r is the radius of the laser beam and $r = 50$ μm. Such a Gaussian profile is chosen by fitting the spatial profile of the laser beam determined from experimental tests [53]. The angle of incidence is 0° (i.e., the laser beam is perpendicular to the target surface). Ablation of the aluminum target after a single laser pulse was observed throughout this study.

4.1 Comparison between predictions and experimental data

The ablation depths of the aluminum target predicted using the proposed model at laser irradiances of 0.45, 1.11, and 1.92 GW/cm² for a 193 nm Excimer laser were compared with the results predicted using our early model without considering the plasma-shielding effect [27] and the experimental data [54], as shown in Fig. 2. Note that since the ablation continues after the laser source was removed from the target surface, the ablation depths at the end of the cooling step were obtained in this study. The continuation of ablation followed by the removal of the laser pulse has been observed in the experimental test [11] and also found in theoretical analyses [27, 55]. Our simulation results show that the ablation continued for 13.9 ns, 12.5 ns, and 5.8 ns at laser irradiances of 0.45, 1.11, and 1.92 GW/cm², respectively, for the 193 nm laser. It can be seen from Fig. 2 that the ablation depths, when compared to those predicted without considering the plasma-shielding effect, underwent a reduction of 3.23%, 2.87%, and 2.55% at laser irradiances of 0.45, 1.11, and 1.92 GW/cm², respectively. These reductions are direct

evidences of the attenuation of the laser heat flux owing to the plasma-shielding effect. Despite the reductions, the predictions still showed good agreement with the experimental data.

Similarly, the ablation depths of the aluminum target at laser irradiances of 1.71, 2.29, 2.95, and 3.78 GW/cm² for a 266 nm Nd:YAG laser were also obtained using the proposed model. The comparison of the ablation depths predicted with and without considering the plasma-shielding effect, the experimental test data, and those predicted based a hydrodynamic method is provided in Fig. 3. The reductions of the predicted ablation depths are 7.40%, 8.16%, 8.83%, and 9.42% at the laser irradiances of 1.71, 2.29, 2.95, and 3.78 GW/cm², respectively, due to the plasma-shielding effect. The difference between the current predictions considering the plasma-shielding effect and the experimental data is 9.47%, 8.33%, and 19.6% at laser irradiances of 2.29, 2.95, and 3.78 GW/cm², respectively. It is worth mentioning that the exact modeling predictions can be influenced by various factors, such as the uncertainties in the material properties, especially at extreme high temperatures. For example, the material properties above the boiling temperature (e.g., 2743 K for aluminum) can generally only be obtained through theoretical analysis, since no available experimental measurements exist due to the limitations of the instrumentation. In authors' previous work [43], we found that a 10% change in either the lower or upper bound of the absorption coefficient of the aluminum target can lead to an approximate 1.8% change in the predicted mean ablation depths. Therefore, the exact modeling predictions of the ablation depth for both cases with and without
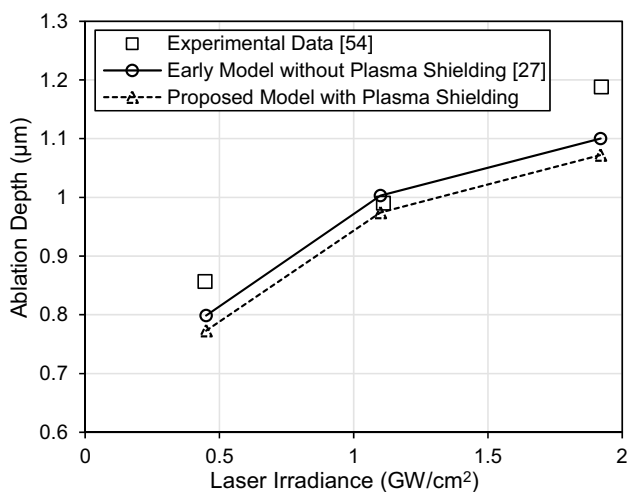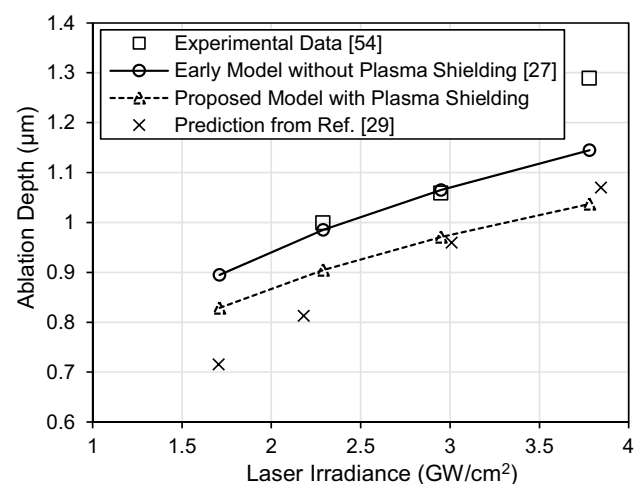

Fig. 2 Ablation depth of the aluminum target (wavelength 193 nm, duration 12 ns, cooling step 350 ns): comparison of predictions with and without considering the plasma-shielding effect and the experimental data [54]

Fig. 3 Ablation depth of the aluminum target (wavelength 266 nm, duration 6 ns, cooling step 350 ns): comparison of predictions with and without considering the plasma-shielding effect, the experimental data [54], and the predictions using a hydrodynamic method [29]

considering the plasma-shielding effect could be affected by such uncertainties in the material properties, possibly leading to slightly lower predictions of the ablation depth in general. Furthermore, despite consistently lower, the current predictions considering the plasma-shielding effect are still in closer agreement with the experimental measurements when compared to other numerical predictions reported by Cao et al. [29], as shown in Fig. 3. Such a comparison proves that our current predictions are still acceptable. Moreover, although the exact predictions of the ablation depth considering plasma-shielding effect appear to be in less agreement with the experimental measurement, the directions reflected from the simulation results are consistent with experimental findings. For example, the predicted ablation depths considering plasma shielding are consistently lower than those predicted without considering the plasma shielding due to the reduced energy passing through the plasma cloud. Such a trend agrees with the experimental findings (see Refs. [18, 22, 23] in the revised manuscript) and other reported simulation results (see Refs. [29–35] in the revised manuscript). Moreover, after taking into account the plasma-shielding effect, the reduction of the ablation depths is only about 2.55–3.23%, indicating that the Bremsstrahlung effect for the UV lasers considered in this study is not significant. This also agrees well with the experimental findings [17].

At the same time, it can be noticed that the reductions of ablation depths for a laser with 266 nm wavelength are higher than those for a laser with 193 nm wavelength, which, however, does not necessarily imply that a longer wavelength augments the plasma-shielding effect. The effect of laser wavelength on the plasma shielding can be explained by checking Eq. (9). The common factor in both formulas of Eq. (9), $1 - \exp\left(-hc/\lambda k_B T\right)$, decreases, as the laser wavelength λ increases. However, on the other hand, the electron-ion IB absorption effect $\alpha_{IB,e-i}$ increases with λ^3. Therefore, the relative contribution of these two opposing combined effects will decide the general outcome of the effect of laser wavelength on the overall absorption of the plasma. Moreover, the change of the optical properties of the target material including the absorptivity and reflectivity at different laser wavelengths also contributes to the change of the mass ablation rate. Many studies have investigated the effect of laser wavelength on the plasma shielding and the mass ablation rate [19, 23, 56]. For example, it has been reported that different mass ablation rates for 1064 nm, 532 nm, and 266 nm laser wavelengths were attributed to plasma shielding occurring as a result of IB processes dominant at longer wavelengths [57]. Furthermore, a numerical model has predicted less plasma shielding at a wavelength of 532 nm when compared to that at a shorter wavelength of 266 nm [56]. Such a finding is not consistent with our calculations for which the plasma-shielding effect seems to be more pronounced for

the longer wavelength 266 nm when compared to the short wavelength 193 nm.

Figure 4 shows the predictions of electron density within the plasma plume along the x-direction (see Fig. 1) of the left half problem domain at five times, $t = 2.6, 3.0, 4.0, 5.0,$ and 6.0 ns at an intensity of 3.78 GW/cm^2 and a wavelength of 266 nm. Figure 5 illustrates the contour plots of the shape change and temperature distributions in the 2D material domain, where Figs. 5(a), (c), and (e) show the distributions predicted considering the plasma-shielding effect using the current proposed model, while Figs. 5(b), (d), and (f) show distributions predicted without considering the plasma-shielding effect using our early model [27].

4.2 Effect of plasma temperature

As described in Sect. 2.2.3, in the proposed model, an averaged plasma temperature was used and taken as 1.5 times of the surface temperature of the target. Figure 6 shows the predicted temperature histories at the center ($x = 0$, see Fig. 1) of the target surface at laser irradiances of 0.45, 1.11, and 1.92 GW/cm^2 for the laser of 193 nm. Note that for the cases of 0.45 and 1.11 GW/cm^2, the surface temperature reached approximately a steady value of 8000 K after $t = 2.8$ μs. This means that a balance has been established between the heat absorption of the material from the laser heating and the heat loss due to the progressive material vaporization. However, for the case with a relatively higher irradiance, 1.92 GW/cm^2, the heat absorption due to the laser heating is initially much higher than the heat loss, which has caused the "bump" in Fig. 6. As the time increases, the heat loss due to the vaporization has caught up again with the heat absorption and finally balanced each other, followed by a steady
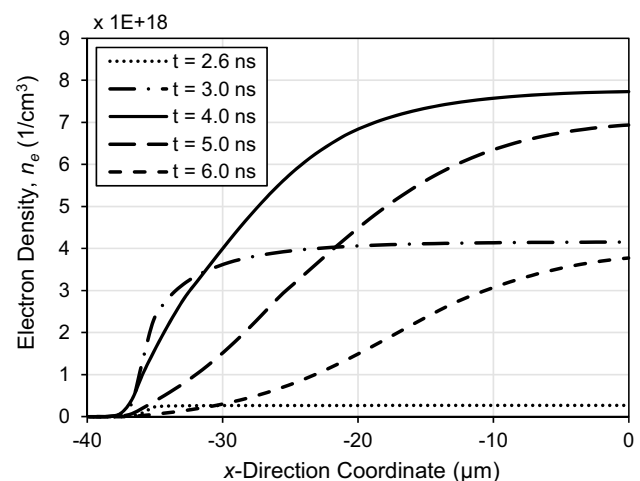
Fig. 4 Electron density within the plasma along the x-direction (see Fig. 1) at $t = 2.6, 3.0, 4.0, 5.0,$ and 6.0 ns (3.78 GW/cm^2, wavelength 266 nm, duration 6 ns, cooling step 350 ns)
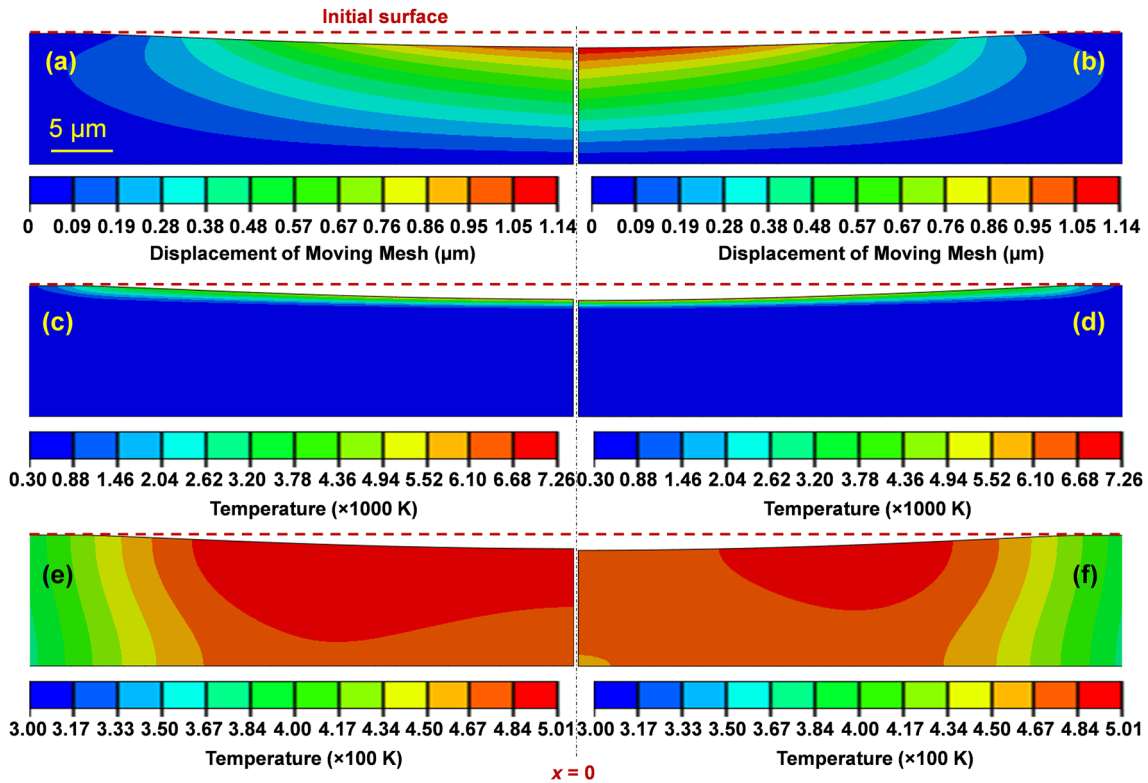
Fig. 5 Contour plots of the shape change and temperature distributions within the aluminum target due to the pulsed laser ablation (3.78 GW/cm^2, wavelength 266 nm, duration 6 ns, cooling step 350 ns): **a**, **c**, and **e** show the shape change at the end of the cooling step, temperature distributions at the end of the laser pulse, and temperature distributions at the end of the cooling step considering the plasma-shielding effect, respectively. **b**, **d**, and **f** are the corresponding outputs without considering the plasma-shielding effect

surface temperature after the "bump". It can be noticed that the surface temperature at its steady state for all three cases is about 8000 K. Therefore, the average plasma temperature

Fig. 6 Temperature histories at the center ($x=0$, see Fig. 1) of the target surface at laser irradiances of 0.45, 1.11, and 1.92 GW/cm^2 (wavelength 193 nm, duration 12 ns, cooling step 350 ns)

is about 12,000 K. Such a plasma temperature is consistent with the calculation predicted in Ref. [56]. Although their predictions are for laser wavelengths of 266 nm and 532 nm, the plasma temperature at 193 nm is expected to be close to that at 266 nm. The plasma temperature of 12,000 K is also quite consistent with the experimental data reported in Ref. [20] for which the temperature of the plasma produced by single and double pulses with steel targets was determined to be 8000–12,000 K in the center of the plasma by tomography using a random transfer technique. In addition, the steady plasma temperature is also consistent with the numerical predictions reported in Ref.[21], although the onset of the steady state is slightly different.
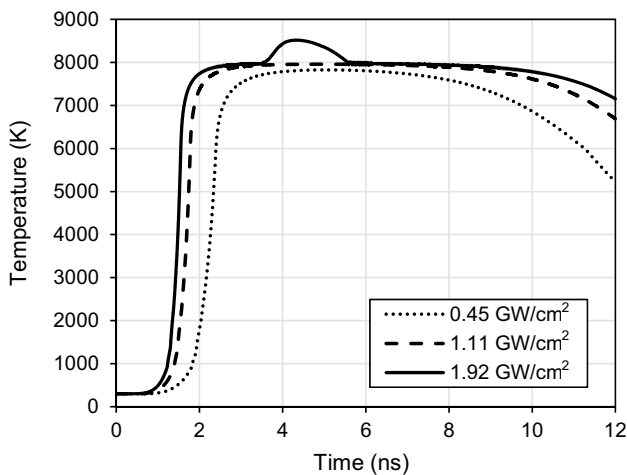
To investigate the effect of the average plasma temperature on the plasma shielding, additional simulations were performed at the laser irradiance of 0.45 GW/cm^2 for the laser of 193 nm when different ratios of the average plasma temperature and the target surface temperature, T_{avg}/T_s, were assumed. The comparison of the temporal profiles of the incident laser irradiance and the transmitted laser irradiance calculated by assuming different T_{avg}/T_s is illustrated in Fig. 7. It can be seen that the attenuation of the laser irradiance at $T_{avg}/T_s = 2$ is negligible when compared to that
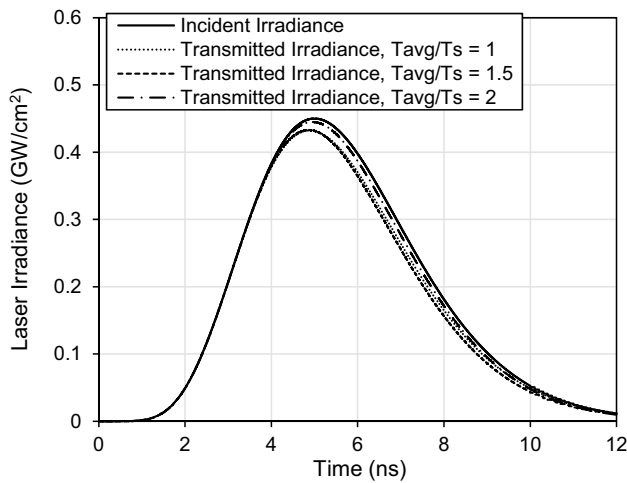
Fig. 7 Temporal profiles of the incident laser irradiance and the transmitted laser irradiance when $T_{avg}/T_s = 1$, 1.5, and 2 were assumed in the model (0.45 GW/cm², wavelength 193 nm, duration 12 ns, cooling step 350 ns)

at $T_{avg}/T_s = 1$ and $T_{avg}/T_s = 1.5$. Furthermore, the energy transmission ratios calculated by assuming different T_{avg}/T_s are plotted in Fig. 8. Here, the energy transmission ratio, ψ, was defined as the ratio between the transmitted laser energy and the incident laser energy, where the transmitted and the incident laser energy were calculated by integrating the transmitted and incident laser irradiance with time, respectively. It can be observed that the transmission ratio does not monotonically increase or decrease as the average plasma temperature increases. In other words, the attenuation of the laser energy due to the plasma-shielding effect does not necessarily monotonically increase or decrease as
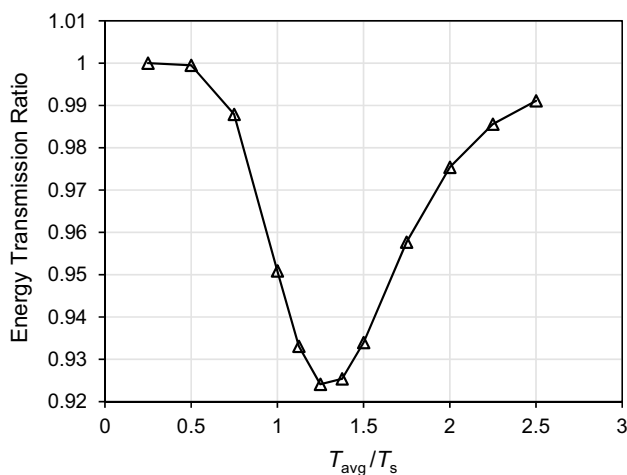
the average plasma temperature increases at a fixed laser irradiance. Moreover, the change in the transmission ratios is also quite low seeing only a 7.6% difference in Fig. 8 between the maximum and the minimum transmission ratios.

To further demonstrate the effect of the plasma temperature on the plasma shielding, four additional cases by assuming constant plasma temperatures of $T_{avg} = 9000$, 10000, 11000, and 12000 K, respectively, were performed. The energy transmission ratios obtained from these four cases were compared with the ratio obtained by assuming that $T_{avg}/T_s = 1.5$, as shown in Fig. 9. It can be noticed that the maximum difference of the energy transmission ratio between the cases with constant plasma temperatures and the case with $T_{avg}/T_s = 1.5$ is about 1.3%. Meanwhile, the transmission ratio obtained for the case with $T_{avg}/T_s = 1.5$ is about the mean of the transmission ratios obtained with constant plasma temperatures. These evidences, in turn, proves that within a reasonable range of the plasma temperature (i.e., 9000—12,000 K), our assumption of $T_{avg}/T_s = 1.5$ used in the proposed model is valid. Hence, the calculated transmission ratio based on our assumption is representative.

4.3 Effect of laser intensity

The effect of the laser intensity on the plasma shielding was investigated through additional simulations at different laser irradiances with a 193 nm laser. Figure 10 shows the calculated transmission ratios at different laser irradiances and the corresponding curve fitting using linear regression. The energy transmission ratio follows an approximate linear function, $\psi = -0.0412 \cdot I + 0.9772$. The ratio decreases with the increase of the laser irradiance. In other words, the plasma-shielding effect becomes more pronounced with
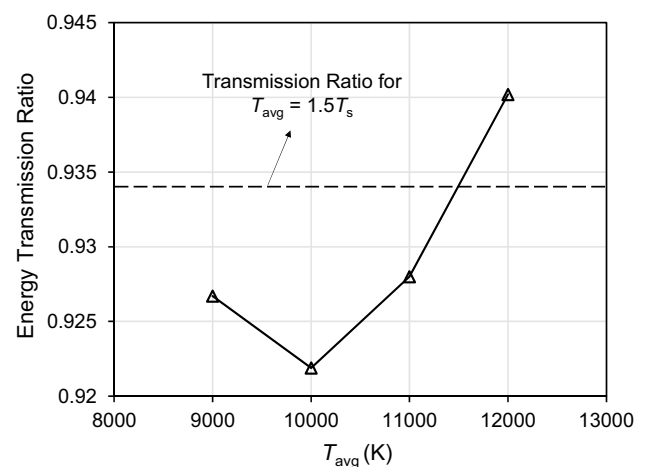

Fig. 8 Laser energy transmission ratios (i.e., ratio between the transmitted laser energy and the incident laser energy) when different T_{avg}/T_s was assumed in the model (0.45 GW/cm², wavelength 193 nm, duration 12 ns, cooling step 350 ns)

Fig. 9 Comparison of energy transmission ratios obtained by assuming a constant plasma temperature (9000, 10,000, 11,000, and 12,000 K) and the ratio obtained by assuming $T_{avg}/T_s = 1.5$ (0.45 GW/cm², wavelength 193 nm, duration 12 ns, cooling step 350 ns)
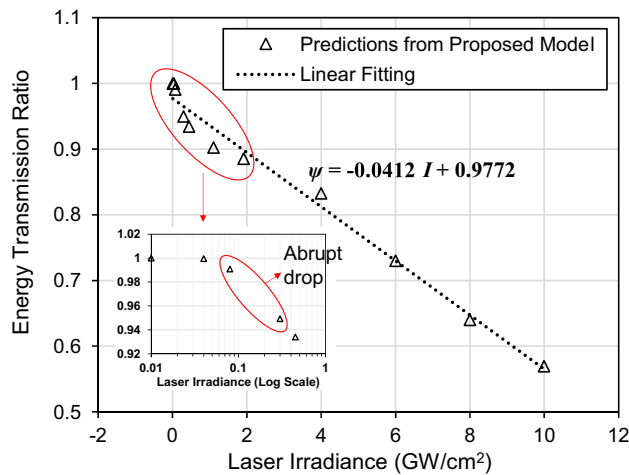
Fig. 10 Laser energy transmission ratios at different laser irradiances (wavelength 193 nm, duration 12 ns, cooling step 350 ns) with an inset showing the energy transmission ratio for 0–2 GW/cm^2 on a logarithmic irradiance scale

Fig. 11 Electron density versus time at the center ($x=0$, see Fig. 1) of the plasma near the target surface at laser irradiances of 0.45, 1.11, and 1.92 GW/cm^2 (wavelength 193 nm, duration 12 ns, cooling step 350 ns)

the increase of the laser irradiance. It can be noticed from Fig. 10 that the transmission ratio dropped by 43% when the laser irradiance increased from 0.01 to 10 GW/cm^2. It is worth mentioning that similar results have been reported in many other studies [21, 58]. For example, a plasma-shielding factor, which was defined as 100% minus the energy transmission ratio, was found to monotonically increase from 0.32 to 0.89 when the laser irradiance was increased from 2 to 8 GW/cm^2 for a 355 nm Nd:YAG laser and a copper sample based on the experimental and simulation results reported by Ref.[21]. Similarly, the experimental test data of the transmitted laser energy (i.e., integral of laser temporal profile with time) versus power density was reported by Ref.[58], in which it was found that transmitted energy increases and fluctuates before the laser power density reaches 0.3 GW/cm^2, and decreases monotonically after the laser energy reaches 0.3 GW/cm^2 for a 248 nm KrF excimer laser and a brass sample. Similar trends can also be observed from our predictions, as shown in Fig. 10. As one can see, an abrupt drop of the energy transmission ratio occurs when the laser irradiance increases from 0.08 to 0.3 GW/cm^2.

Figures 11 and 12 show the electron density, n_e, and the total absorption coefficient, α_{IB}, at the center ($x=0$, see Fig. 1) near the target surface at laser irradiances of 0.45, 1.11, and 1.92 GW/cm^2 for the 193 nm laser. It can be noticed that both the electron density and total absorption coefficient increase as the laser irradiance increases. The order of the electron density predicted using the proposed model is about $\sim 10^{18}$ 1/cm^3, which is consistent with the experimental measurement data determined using spectroscopic techniques [17, 23]. It can also be observed from Fig. 11 that the electron density starts to decrease after about
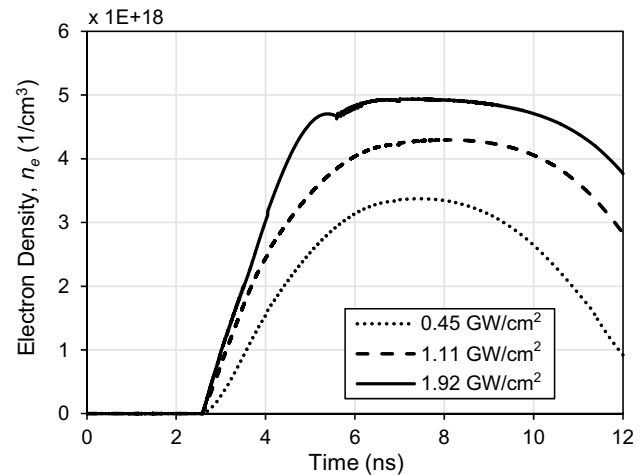
8 ns of the laser pulse and is expected to continue to decrease after the end of laser pulse. Such an observation is also quite consistent with the experimental data reported in Ref. [17], for which the electron density was reported to decrease monotonically from 13 to 175 ns. Moreover, simulation data reported in Ref. [32, 56] also found the electron density increases with the increase of the laser irradiance. At the same time, the decrease of the electron density at later times (see also Fig. 4) was attributed to the increased diffusivity due to the continuous expansion of the plasma plume [56]. Figure 12 shows that the total absorption coefficient due to
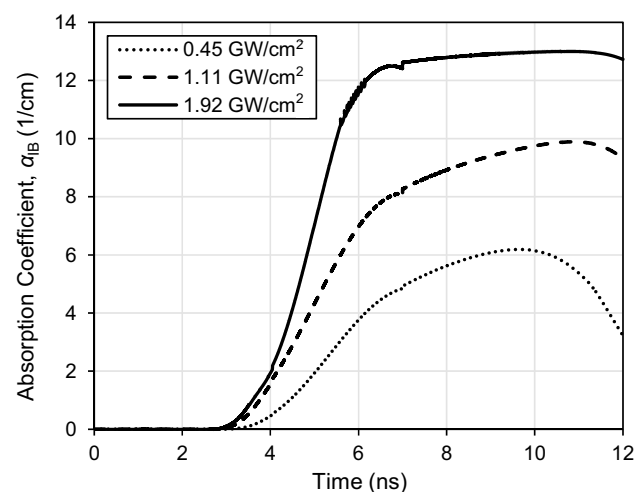

Fig. 12 Total absorption coefficient, α_{IB}, versus time at the center ($x=0$, see Fig. 1) of the target surface at laser irradiances of 0.45, 1.11, and 1.92 GW/cm^2 (wavelength 193 nm, duration 12 ns, cooling step 350 ns)

the IB effect, α_{IB}, increases as the laser irradiance increases. This trend was expected, since the energy transmission ratio shown in Fig. 10 decreases as the laser irradiance increases. At 8 ns for example, the absorption coefficient increased 1.5 times and 2.2 times when the laser irradiance increased from 0.45 to 1.11 GW/cm^2 and from 0.45 to 1.92 GW/cm^2, respectively.

5 Conclusion

In this paper, a 2-D laser heat transfer model was proposed using finite element analysis (FEA) with the commercial FEA software ABAQUS to study the plasma-shielding effect on the PLA of an aluminum target. The assumptions used in the model include the LTE and additional assumptions regarding the average plasma temperature and vapor density, under which the Saha–Eggert equation, conservation equations of matter and charge can be used. Studies have also been carried out to provide justifications to these assumptions. It is worth noting that the proposed model considers the material moving front and captures the progressive shape change simultaneously with the evolution of the temperature field.

The proposed 2-D FE model was employed to study the plasma-shielding effect on PLA of an aluminum target produced by a 193 nm Excimer laser and a 266 nm Nd:YAG laser. The ablation depths predicted considering the plasma-shielding effect were slightly lower than those predicted without considering the plasma-shielding effect at the laser intensities we investigated. Due to the small difference, both predictions showed good agreement with the experimental data. The small difference could be due to the insignificant Bremsstrahlung effect for the laser wavelengths of 193 and 266 nm at the plasma temperatures considered in the current model. Future work will look into other mechanisms of the plasma absorption, such as the electron recombination or line contributions. When the laser intensity increases, the plasma-shielding effect becomes more pronounced as evidenced by the effect of laser intensity on the laser energy transmission ratio (i.e., ratio between transmitted laser energy and incident laser energy). It was found that the transmission ratio decreases almost linearly with the increase of the laser intensity. Moreover, an abrupt drop of the transmission ratio was observed at a laser intensity of 0.3 GW/cm^2. Such a finding was also consistent with experimental data. The evolutions of electron density and plasma temperature were also obtained, and their orders of magnitude also showed good agreement with the experimental data.

To summarize, the proposed 2D laser heat transfer simple model provides a capability of estimating the evolutions of electron density and plasma temperature in addition to predicting the evolutions of temperature field and ablation profiles using FEA with ABAQUS. While it is still more rigorous and accurate to solve both energy balance equations in the plasma domain and the solid domain using, for example, the hydrodynamic model, the proposed FE model allows to solve a less number of nonlinear equations, and hence, is more computationally efficient, especially for problems with 2-D and 3-D geometries. The proposed model is currently limited to a simple plasma composition and plasma absorption mechanisms of ionization and IB absorption. Future work will be carried out to investigate possible ways to solve both energy balance equations in the solid and plasma domains with ABAQUS and incorporate the additional plasma absorption mechanisms into the model.

References

1. H. Ding, Y.C. Shin, Laser-assisted machining of hardened steel parts with surface integrity analysis. Int J Mach Tools Manuf **50**(1), 106–114 (2010)
2. A.M. Morales, C.M. Lieber, A laser ablation method for the synthesis of crystalline semiconductor nanowires. Science **279**(5348), 208–211 (1998)
3. P. Parandoush, L. Tucker, C. Zhou, D. Lin, Laser assisted additive manufacturing of continuous fiber reinforced thermoplastic composites. Mater Des **131**, 186–195 (2017)
4. N. Shen, H. Ding, Q. Wang, H. Ding, Effect of confinement on surface modification for laser peen forming without protective coating. Surf Coat Technol **289**, 194–205 (2016)
5. J. Liu, S. Suslov, Z. Ren, Y. Dong, C. Ye, Microstructure evolution in Ti64 subjected to laser-assisted ultrasonic nanocrystal surface modification. Int J Mach Tools Manuf **136**, 19–33 (2019)
6. M.N.R. Ashfold, F. Claeyssens, G.M. Fuge, S.J. Henley, Pulsed laser ablation and deposition of thin films. Chem Soc Rev **33**(1), 23–31 (2004)
7. L.M. Shanyfelt, P.L. Dickrell, H.F. Edelhauser, D.W. Hahn, Effects of laser repetition rate on corneal tissue ablation for 193-nm excimer laser light. Lasers Surg Med **40**(7), 483–493 (2008)
8. D.W. Hahn, N. Omenetto, Laser-induced breakdown spectroscopy (LIBS), part I: review of basic diagnostics and plasma–particle interactions: still-challenging issues within the analytical plasma community. Appl Spectrosc **64**(12), 335A–366A (2010)
9. N.M. Bulgakova, A.V. Bulgakov, Pulsed laser ablation of solids: transition from normal vaporization to phase explosion. Appl Phys A Mater Sci Process **73**(2), 199–208 (2001)
10. G. Cristoforetti, S. Legnaioli, V. Palleschi, E. Tognoni, P.A. Benedetti, Observation of different mass removal regimes during the laser ablation of an aluminium target in air. J Anal At Spectrom **23**(11), 1518–1528 (2008)

11. C. Porneala, D.A. Willis, Observation of nanosecond laser-induced phase explosion in aluminum. Appl Phys Lett **89**(21), 211121 (2006)

12. J.M. Fishburn, R.P. Mildren, D. Kapitan, M.J. Withford, D.J.W. Brown, J.A. Piper, Exploring the explosive ablation regime of metals in nanosecond micromachining, in: Proceeding of the SPIE 3885, High-Power Laser Ablation II, (2000) pp. 453–460.

13. Y. Wang, D. Diaz, D.W. Hahn, Ablation characteristics of nanosecond laser pulsed ablation of aluminum, in: ASME International Mechanical Engineering Congress and Exposition, Pittsburgh, 2018, pp. V002T002A086–V002T002A086.

14. X. Zhao, Y.C. Shin, Laser–plasma interaction and plasma enhancement by ultrashort double-pulse ablation. Appl Phys B **120**(1), 81–87 (2015)

15. X. Zeng, X. Mao, S.S. Mao, S.-B. Wen, R. Greif, R.E. Russo, Laser-induced shockwave propagation from ablation in a cavity. Appl Phys Lett **88**(6), 061502 (2006)

16. J.C. Miller, R.F. Haglund, *Laser ablation and desorption* (Academic Press, London, 1998)

17. A.E. Hussein, P.K. Diwakar, S.S. Harilal, A. Hassanein, The role of laser wavelength on plasma generation and expansion of ablation plumes in air. J Appl Phys **113**(14), 143305 (2013)

18. X. Zeng, X.L. Mao, R. Greif, R.E. Russo, Experimental investigation of ablation efficiency and plasma expansion during femtosecond and nanosecond laser ablation of silicon. Appl Phys A **80**(2), 237–241 (2005)

19. M.S. Dawood, A. Hamdan, J. Margot, Influence of surrounding gas, composition and pressure on plasma plume dynamics of nanosecond pulsed laser-induced aluminum plasmas. AIP Adv **5**(10), 107143 (2015)

20. S. Eschlböck-Fuchs, A. Demidov, I.B. Gornushkin, T. Schmid, R. Rössler, N. Huber, U. Panne, J.D. Pedarnig, Tomography of homogenized laser-induced plasma by Radon transform technique. Spectrochim Acta Part B **123**, 59–67 (2016)

21. S. Nammi, N.J. Vasa, B. Gurusamy, A.C. Mathur, Single laser based pump-probe technique to study plasma shielding during nanosecond laser ablation of copper thin films. J Phys D Appl Phys **50**(35), 355204 (2017)

22. M. Ribière, B.G. Chéron, Analysis of relaxing laser-induced plasmas by absorption spectroscopy: Toward a new quantitative diagnostic technique. Spectrochim Acta Part B **65**(7), 524–532 (2010)

23. O. Barthélemy, J. Margot, M. Chaker, M. Sabsabi, F. Vidal, T.W. Johnston, S. Laville, B. Le Drogoff, Influence of the laser parameters on the space and time characteristics of an aluminum laser-induced plasma. Spectrochim Acta Part B **60**(7–8), 905–914 (2005)

24. A. Gragossian, S.H. Tavassoli, B. Shokri, Laser ablation of aluminum from normal evaporation to phase explosion. J Appl Phys **105**(10), 103304 (2009)

25. V. Oliveira, R. Vilar, Finite element simulation of pulsed laser ablation of titanium carbide. Appl Surf Sci **253**(19), 7810–7814 (2007)

26. N.A. Vasantgadkar, U.V. Bhandarkar, S.S. Joshi, A finite element model to predict the ablation depth in pulsed laser ablation. Thin Solid Films **519**(4), 1421–1430 (2010)

27. Y. Wang, N. Shen, G.K. Befekadu, C.L. Pasiliao, Modeling pulsed laser ablation of aluminum with finite element analysis considering material moving front. Int J Heat Mass Transf **113**, 1246–1253 (2017)

28. B. Kim, R. Iida, D.H. Doan, K. Fushinobu, Nanosecond pulse laser scribing using Bessel beam for single shot removal of transparent conductive oxide thin film. Int J Heat Mass Transf **107**, 829–835 (2017)

29. Y. Cao, X. Zhao, Y.C. Shin, Analysis of nanosecond laser ablation of aluminum with and without phase explosion in air and water. J Laser Appl **25**(3), 032002 (2013)

30. T. Moscicki, J. Hoffman, Z. Szymanski, Laser ablation in an ambient gas: modelling and experiment. J Appl Phys **123**(8), 083305 (2018)

31. Y. Zhang, D. Zhang, J. Wu, Z. He, X. Deng, A thermal model for nanosecond pulsed laser ablation of aluminum. AIP Adv **7**(7), 075010 (2017)

32. A. Bogaerts, Z. Chen, R. Gijbels, A. Vertes, Laser ablation for analytical sampling: what can we learn from modeling? Spectrochim Acta Part B **58**(11), 1867–1893 (2003)

33. J.K. Antony, G.S. Jatana, N.J. Vasa, V.L.N.S. Raja, A.S. Laxmiprasad, Modeling of laser induced breakdown spectroscopy for very low-pressure conditions. Appl Phys A **101**(1), 161–165 (2010)

34. S. Tao, Y. Zhou, B. Wu, Y. Gao, Infrared long nanosecond laser pulse ablation of silicon: Integrated two-dimensional modeling and time-resolved experimental study. Appl Surf Sci **258**(19), 7766–7773 (2012)

35. A.V. Gusarov, I. Smurov, Near-surface laser–vapour coupling in nanosecond pulsed laser ablation. J Phys D Appl Phys **36**(23), 2962 (2003)

36. A.V. Bulgakov, N.M. Bulgakova, Thermal model of pulsed laser ablation under the conditions of formation and heating of a radiation-absorbing plasma. Quantum Electron **29**(5), 433 (1999)

37. N.M. Bulgakova, A.V. Bulgakov, L.P. Babich, Energy balance of pulsed laser ablation: thermal model revised. Appl Phys A **79**(4–6), 1323–1326 (2004)

38. D.A. Willis, X. Xu, Heat transfer and phase change during picosecond laser ablation of nickel. Int J Heat Mass Transf **45**(19), 3911–3918 (2002)

39. V. Morel, A. Bultel, B.G. Chéron, The critical temperature of aluminum. Int J Thermophys **30**(6), 1853–1863 (2009)

40. J.H. Yoo, S.H. Jeong, R. Greif, R.E. Russo, Explosive change in crater properties during high power nanosecond laser ablation of silicon. J Appl Phys **88**(3), 1638–1649 (2000)

41. X. Jia, X. Zhao, Numerical study of material decomposition in ultrafast laser interaction with metals. Appl Surf Sci **463**, 781–790 (2019)

42. Y. Cao, Ablation and plasma effects during nanosecond laser matter interaction in air and water. PhD Thesis, Purdue University, 2015.

43. Y. Wang, G.K. Befekadu, H. Ding, D.W. Hahn, Uncertainty quantification for modeling pulsed laser ablation of aluminum considering uncertainty in the temperature-dependent absorption coefficient. Int J Heat Mass Transf **120**, 515–522 (2018)

44. S. Ghalamdaran, P. Parvin, M.J. Torkamany, J.S. Zadeh, Two-dimensional simulation of laser ablation with 235 nanosecond pulses. J Laser Appl **26**(1), 012009 (2014)

45. T. Sakai, Impulse generation on aluminum target irradiated with Nd: YAG laser pulse in ambient gas. J Propul Power **25**(2), 406–414 (2009)

46. Y.B. Zel'Dovich, Y.P. Raizer, *Physics of shock waves and high-temperature hydrodynamic phenomena* (Dover Publications Inc, New York, 2012)

47. Y. Wang, C.L. Pasiliao, Modeling ablation of laminated composites: a novel manual mesh moving finite element analysis procedure with ABAQUS. Int J Heat Mass Transf **116**, 306–313 (2018)

48. Y. Wang, O.I. Zhupanska, Modeling of thermal response and ablation in laminated glass fiber reinforced polymer matrix composites due to lightning strike. Appl Math Model **53**, 118–131 (2018)

49. Y. Wang, Multiphysics analysis of lightning strike damage in laminated carbon/glass fiber reinforced polymer matrix composite

materials: A review of problem formulation and computational modeling. Compos A Appl Sci Manuf **101**, 543–553 (2017)

50. Y. Wang, O.I. Zhupanska, Lightning strike thermal damage model for glass fiber reinforced polymer matrix composites and its application to wind turbine blades. Compos Struct **132**, 1182–1191 (2015)

51. Y. Wang, T.K. Risch, C.L. Pasiliao, Modeling of Pyrolyzing ablation problem with ABAQUS: a one-dimensional test case. J Thermophys Heat Transfer **32**(2), 544–546 (2017)

52. B.-L. Chua, H.-J. Lee, D.-G. Ahn, Y. Wang, A study on activation algorithm of finite elements for three-dimensional transient heat transfer analysis of directed energy deposition process. Int J Precis Eng Manuf **20**(5), 863–869 (2019)

53. E. Assuncao, S. Williams, Effect of material properties on the laser welding mode limits. J Laser Appl **26**(1), 012008 (2014)

54. I. Horn, M. Guillong, D. Günther, Wavelength dependant ablation rates for metals and silicate glasses using homogenized laser beam profiles—implications for LA-ICP-MS. Appl Surf Sci **182**(1), 91–102 (2001)

55. G.M. Pound, Selected values of evaporation and condensation coefficients for simple substances. J Phys Chem Ref Data **1**(1), 135–146 (1972)

56. Q. Lu, S.S. Mao, X. Mao, R.E. Russo, Theory analysis of wavelength dependence of laser-induced phase explosion of silicon. J Appl Phys **104**(8), 083301 (2008)

57. A. Bogaerts, Z. Chen, Effect of laser parameters on laser ablation and laser-induced plasma formation: A numerical modeling investigation. Spectrochim Acta Part B **60**(9–10), 1280–1307 (2005)

58. X.L. Mao, A.C. Ciocan, O.V. Borisov, R.E. Russo, Laser ablation processes investigated using inductively coupled plasma–atomic emission spectroscopy (ICP–AES). Appl Surf Sci **127**, 262–268 (1998)

59. X. Mao, R.E. Russo, Invited paper—observation of plasma shielding by measuring transmitted and reflected laser pulse temporal profiles. Appl Phys A **64**(1), 1–6 (1996)